Supplementary Materials for Multifunctional Interleaved Geometric Phase Dielectric Metasurfaces

Elhanan Maguid[1], Igor Yulevich[1], Michael Yannai[1],Vladimir Kleiner[1], Mark Luitzen Brongersma[2], Erez Hasman[1†]

[1]Micro and Nanooptics Laboratory, Faculty of Mechanical Engineering, and Russell Berrie Nanotechnology Institute, Technion – Israel Institute of Technology, Haifa 32000, Israel.

[2]Geballe Laboratory for Advanced Materials, Stanford University, 476 Lomita Mall, Stanford, CA 94305, USA.

[†]Corresponding author. E-mail: mehasman@technion.ac.il

S1. Angular resolution and channel efficiency of interleaved geometric phase metasurfaces

The angular resolution characteristics of the modes generated by interleaved geometric phase metasurfaces (GPMs) were experimentally examined via far-field measurements (Fig. S1, a to h). We show that increasing the number of interleaved channels, *N*, does not affect the mode's angular resolution. Therefore, a constant angular width of approximately λ / D was observed for GPMs generating 4, 9 and 16 channels, matching the diffraction-limited angular resolution of a shared-aperture GPM of size *D* (Fig. S1i).

In order to estimate the impact of an incrementally growing number of wavefronts on the intensity per channel, the far-field intensity distributions were experimentally measured and simulated (finite-difference time-domain, FDTD) for the aforementioned GPMs, in agreement with Fourier calculation and Wigner distribution in phase-space (Fig. S1j). Our results show that the intensity per channel scales as $1/N^2$. Note, the intensity of each channel in the GPM of *N* interleaved phase functions $I^{(N)}$ was normalized by a single channel intensity $I^{(1)}$. Moreover, the aforementioned experiments were also used to measure the *SNR* (Fig. 1f) as a function of the total number of interleaved channels *N*.

S2. Wavelength-independent vortex singularities

Geometric phase metasurfaces can operate within a broad wavelength range. The geometric phase-pickup, $2\sigma\theta(x, y)$, acquired by space-variant anisotropic Si building-blocks depends only on the incident spin and the local orientation angle $\theta(x, y)$ of the nanoantennas. Hence, the geometric phase profile is wavelength independent. This property is experimentally demonstrated by illuminating the interleaved GPM (Fig. 1a) with circularly polarized light at several operating wavelengths, which results in various orbital angular momentum (OAM)

wavefronts (Fig. S2, a to f). Unlike diffractive spiral phase elements the observed diffraction patterns, generated by the GPM, maintains the singular vortex behavior at various wavelengths, verifying the achromatic nature of the spiral geometric phase. Moreover, the interleaved OAM wavefronts manifest diffraction limited spot-sizes which correspond to the shared-aperture diameter, *D* (Fig. S2g).

S3. Wigner phase-space distribution of interleaved geometric phase metasurfaces

Figure S3 illustrates the marginal density functions of the Wigner distribution, $\rho_\sigma^{(N)}(\mathbf{x}) = \int W_\sigma^{(N)}(\mathbf{x},\mathbf{k})d\mathbf{k}$, $\pi_\sigma^{(N)}(\mathbf{k}) = \int W_\sigma^{(N)}(\mathbf{x},\mathbf{k})d\mathbf{x}$, $\tau_\sigma^{(N)}(x,k_x) = \int W_\sigma^{(N)}(\mathbf{x},\mathbf{k})dydk_y$ $\tau_\sigma^{(N)}(y,k_y) = \int W_\sigma^{(N)}(\mathbf{x},\mathbf{k})dxdk_x$, where $\mathbf{x} = (x,y)$ and $\mathbf{k} = (k_x,k_y)$, corresponding to position, momentum and position-momentum spaces, respectively. The calculations were performed for interleaved GPMs of diameter $D = 40\mu m$ generating $N = 4$ and $N = 25$ channels, respectively, where the total number $n \times n$ of nanoantennas is 80x80. Note, the marginal density functions of the Wigner distribution depict more distinguishable channels for 4 modes compared to 25.

S4. Spin-dependent asymmetric harmonic response

We designed a shared-aperture GPM based on a spin-dependent asymmetric harmonic response (HR) approach[4]. The geometric phase function ϕ_g can be designed to obtain spin-dependent OAM harmonic diffraction orders $A_l \exp\left[il\sigma(kx+\varphi)\right]$, where $l\sigma k$ provides the momentum redirection of the *l-th* order. The resultant phase function can be optimized to achieve identical maximal efficiencies $|A_l|^2 \approx 1/(b-a+1)$ for selected asymmetric orders $a < l < b$. We modified the solution proposed by Dammann[33], to realize a GPM providing off-axis spin-dependent asymmetric OAM harmonic orders. The GPM was illuminated with right and left circularly

polarized light and spin-dependent diffraction patterns consisting of multiple OAM orders of $l = 0, \pm 1, \pm 2, \pm 3, \pm 4$ were observed (Fig. S4).

S5. Optical rotatory dispersion and specific rotation

Utilizing the observed diffraction patterns of vectorial vortices we obtained the optical rotatory dispersion (ORD) for the specific rotations $[\alpha]_{\lambda}^{T} = \vartheta / \ell c$ of optically active solution. The specific rotation, for a temperature *T* and wavelength λ, is defined as the change in the polarization angle of linearly polarized light, ϑ (deg), as it passes through a sample of one decimeter length with a concentration of $c = 1g / mL$. In the main text, the optically active solutions are (S)-(-)-Limonene and (R)-(+)-Limonene manufactured by Sigma-Aldrich (CAS 5989-54-8, 5989-27-5), where their ORD was measured using a quartz cuvette of $\ell = 2cm$ at room temperature. Note, the concentrations were 0.844 g/mL and 0.842 g/mL for (S)-(-)-Limonene and (R)-(+)-Limonene, respectively.

The diffraction patterns of $l = 1$ provides the ORD measurement with improved spectral resolvance, whereas the $l = 2$ vectorial vortex improves the rotatory accuracy. Figure 2 in the main text elucidates these improvements by the illustration of the enlarged spots, the spot sizes of $l = 1$ vortex beams are smaller compared to those of $l = 2$, hence, a better wavelength discrimination can be observed. However, the diffraction pattern of $l = 2$ vortex possesses a petal-shape of a higher order (two perpendicular fringes), thus enabling a more accurate determination of the rotatory angle.

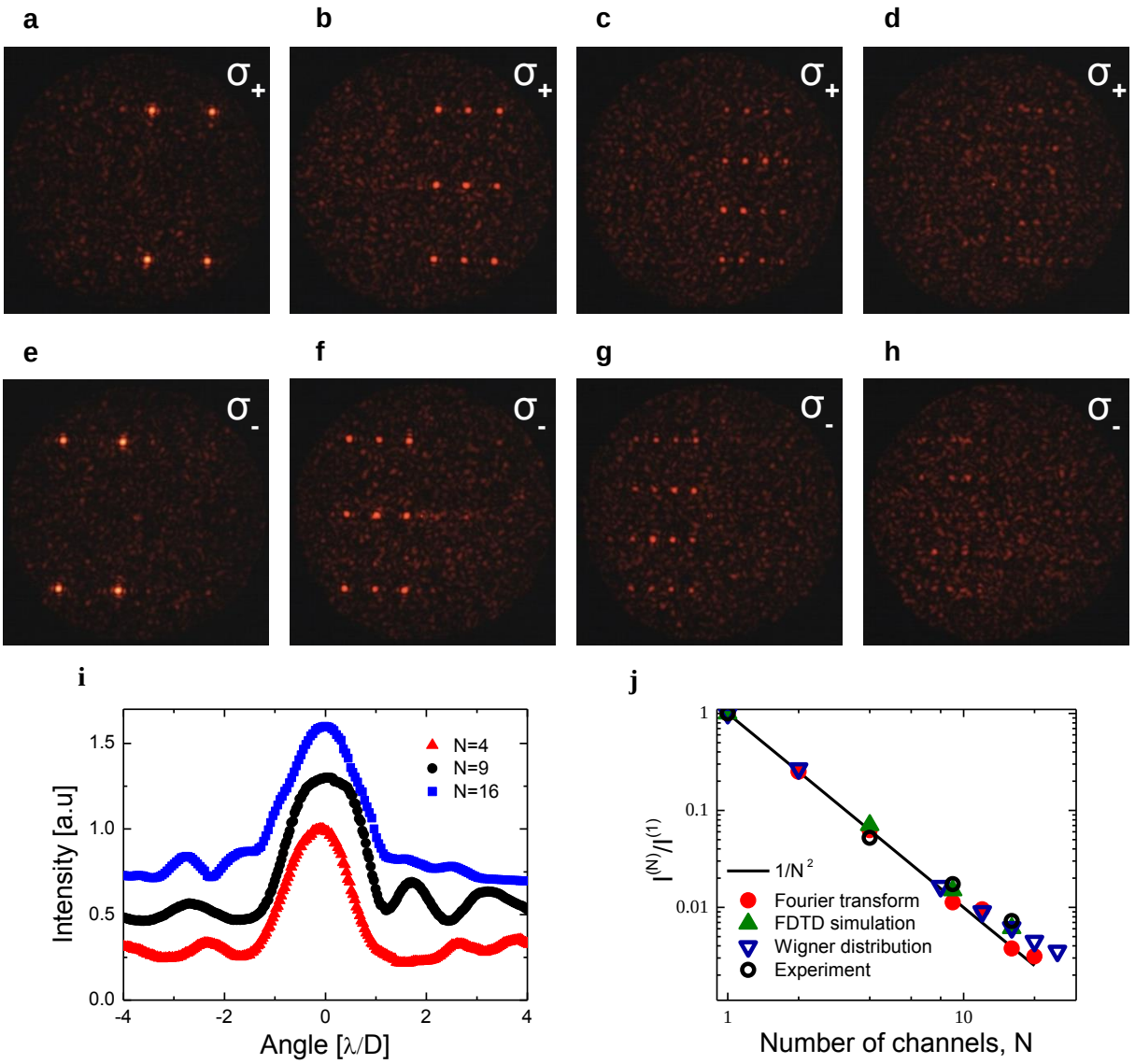

Figure S1. Generation of multiple channels by interleaved GPMs. (**a**-**h**) Measured spin dependent momentum deviations for interleaved GPMs illuminated at a wavelength of 650nm, generating 4 (**a** and **e**), 9 **(b** and **f)**, 16 **(c** and **g)**, and 25 channels **(d** and **h)**. **i**, The corresponding angular width of the interleaved channels, calculated for σ_+ illumination. **j**, Normalized intensity per channel (logarithmic scale) obtained from the experiment depicted from **a** to **d** (black rings) and FDTD simulation (green), whereas the red dots and blue triangles denote the Fourier transform and Wigner distribution calculations, respectively; the line corresponds to ~$1/N^2$.

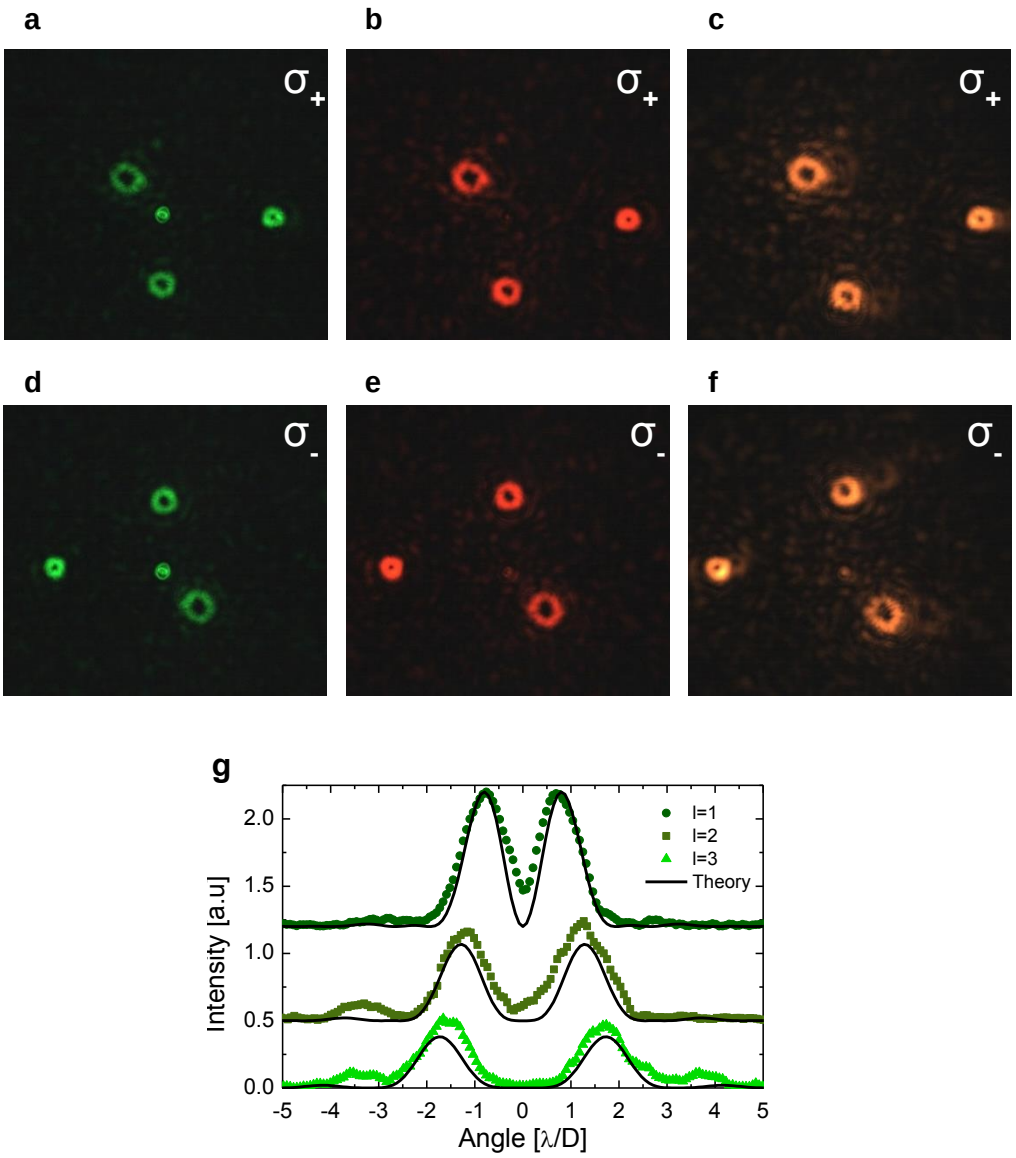

Figure S2. Wavelength-independent OAM wavefronts. (**a**-**f**) Measured spin-flip momentum deviation of three wavefronts with various OAMs at wavelengths of 540nm (**a** and **d**), 630nm (**b** and **e**), and 720nm (**c** and **f**); $\sigma_{\pm}$ denotes the incident spin. **g**, Observed angular width of OAM wavefronts emerging from the interleaved GPM, obtained from the diffraction pattern corresponding to σ_{+} illumination at a wavelength of 540nm.

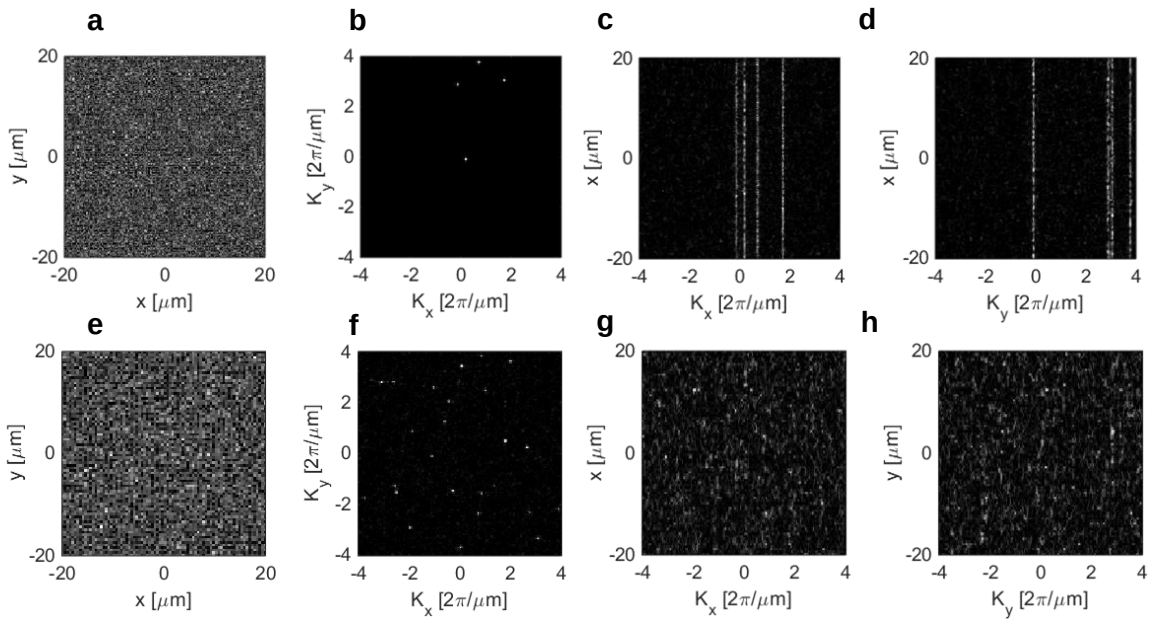

Figure S3. Wigner distributions of interleaved GPMs. (a-h) Calculations showing the Wigner phase-space density functions in position (**a** and **e**), momentum (**b** and **f**) and position-momentum (**c** and **g**, **d** and **h**) space. The calculations were performed for an interleaved GPM of 4 channels (**a** to **d**) and 25 channels (**e** to **h**), and σ_+ illumination, using the normalized aperture size of $D/\lambda = 50$.

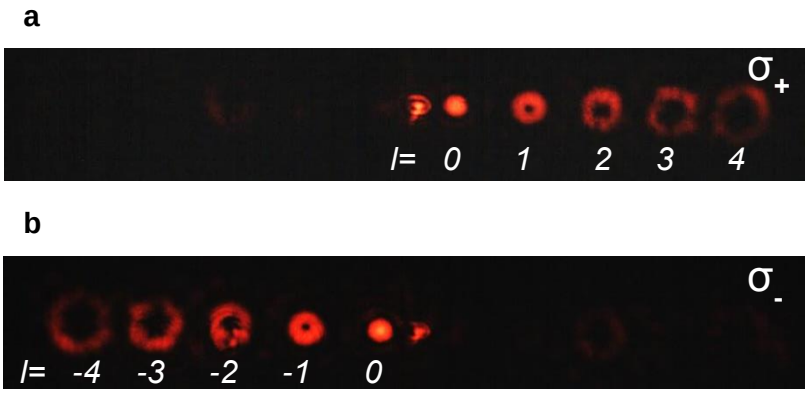

Figure S4. Spin-controlled asymmetric harmonic response GPM. (**a-b**), Measured spin-controlled HR diffraction patterns of five OAM orders, for right (**a**) and left (**b**) circular polarization illumination at a wavelength of 650nm.